Modelling Effect of Rain on the External Aerodynamics of the Utility Truck with the Morphing Boom Equipment: Computations and Wind Tunnel Testing

Parth Y. Patel[1], Chandramouli Krishnamurthy[2], Gavin Clausman[3]
Vladimir V. Vantsevich[4], Roy Koomullil[5]

University of Alabama at Birmingham, Birmingham, Alabama, 35294, USA

Road accidents caused by heavy rain have become a frightening issue in recent years requiring investigation. In this regard, an aerodynamic comparative and experimental rain study is carried out to observe the flow phenomena change around a generic ground vehicle (Ahmed Body at a scale) and the utility truck. In this paper, a Discrete Phase Model (DPM) based computational methodology is used to estimate the effect of rain on aerodynamic performance. First, an experimental rain study of the Ahmed body at a scale that is representative of a car or light truck was conducted at the Wall of Wind (WOW) large-scale testing facility using force measurement equipment. In addition, the experiment allowed drag, lift, and side-force coefficients to be measured at yaw angles up to 55 degrees. Next, experimental results are presented for the Ahmed Body back angle of 35 degrees, then compared to validate the computational model for ground vehicle aerodynamics. Afterwards, we investigated the effect of heavy rainfall (LWC = 30 g/m^3) on the external aerodynamics of the utility truck with the morphing boom equipment using the validated computational fluid dynamics method, and the external flow is presented using a computer visualization. Finally, force & moment coefficients and velocity distributions around the utility truck are computed for each case, and the results are compared.

Keywords: Experimental Wind-Driven Rain Wind Tunnel Testing, Heavy Rainfall, The Ahmed Body, Utility Truck, Morphing Boom Equipment, Discrete Phase Model (DPM), Automotive Aerodynamics, Computational Fluid Dynamics (CFD)

I. Nomenclature

C_d	Drag coefficient
d	Rain droplet size (mm)
d_p	Particle diameter (mm)
DPM	Discrete Phase Model
LES	Large Eddy Simulations
LWC	Liquid Water Content (g/m^3)
R	Rainfall rate (mm/hr)
Re	Reynolds number
URANS	Unsteady Reynolds averaged Navier Stokes
$\vec{u}$	Fluid phase velocity (m/s)
$\vec{u}_p$	Particle velocity (m/s)

μ	Molecular viscosity of the fluid (kg/m·s)
μ_t	Eddy viscosity (kg/m·s)
WOW EF	Wall of Wind Experimental Facility
V_T	Terminal velocity (m/s)
ρ	Fluid density (kg/m^3)
ρ_p	Density of the particle (kg/m^3)

II.Introduction

As the earth's climate has warmed, a new pattern of more frequent and intense weather events has emerged. Global warming increases water vapor in the atmosphere, which can lead to more frequent heavy rain and snowstorms [1]. As a result of the warmer and more humid atmosphere over the oceans, the strongest hurricanes are likely to be more intense, produce more rainfall, and possibly be more prominent. Furthermore, global warming raises sea levels, increasing the amount of seawater and rainfall pushed onto the shore during coastal storms. This seawater, combined with additional rainfall, can potentially cause catastrophic flooding and, most likely, intensify hurricanes and cause severe damage to both residential and public properties. Therefore, the safety of the rescue and repair team is of paramount importance while they attend to emergencies due to these severe weather conditions.

Utility trucks (also known as boom trucks) are the first responders in these extreme climate and weather situations from cutting trees to restoring traffic, recovering living beings from destroyed properties, repairing electric posts, and restoring power. A stable utility truck will be beneficial under this kind of situation, making the utility truck remain on the ground without skidding or even driving on the road to attend to such emergencies. According to the US Census Bureau, there are approximately 15 million trucks currently in operation across the country operated by 2.83 million drivers, 28.2% of whom drive various utility trucks [2]. Such trucks with morphing capabilities of the manipulator can increase the possibility of road accidents in several ways and create hazardous situations on the roads and off-road conditions while moving and performing critical tasks. Recent advancements in the automotive industry necessitate detailed three-dimensional flow analysis to design an optimized structure to minimize aerodynamic resistance and specific fuel consumption. Flow analysis also improves controllability, which lowers accident rates. The aerodynamic fluid flow properties play a significant role in its aerodynamic performance characterized by separated flows [3].

In a rainy environment, wake zones are highly manipulated, resulting in aerodynamic penalties that increase relative accident rates. These change in aerodynamic flow properties were first analyzed by Ahmed et al. [4]. They investigated and compared the time-averaged vortices' nature by varying back angles from 0^0 to 35^0. They concluded that the total drag faced by generic vehicles appears from the resultant pressure gradient of the front and rear. However, they also mentioned that significant flow properties variation could be seen after a 25^0 back angle. Bayraktar et al. [5] considered the Ahmed body at a scale of 4.7 times as a representative of a car or light truck at highway speeds and explored the influence of three back angles of 0-, 12.5-, and 25 degrees. They observed that the drag coefficient only changes about 3.5% in the range of Reynolds numbers from 2.2M to 13.2M. Lienhart et al. [6] worked on 25^0 and 35^0 back angles of the Ahmed body for a comprehensive investigation at the rear end. Mathey et al. [7] got a good agreement on RANS/LES interfaces with the experimental studies while comparing with the mean velocity at the end. Fares et al. [8] employed the Lattice Boltzmann approach and mentioned the requirement of higher density meshes for actual vehicles due to the curvy body shape. Minguez et al. [9] applied the SVV-LES model for the first time to analyze the 25^0 back angle and suggested a better description is possible for the flow dynamics at the roof end. Parth et al. [10] investigated very first time the modelling effect of rain by using two different rain intensities (19 & 30 g/m^3) on the aerodynamic performance of the Ahmed body with a back angle of 25^0 and 35^0. They concluded that the drag coefficient increases as the rain intensity increases. Thus, it can be inferred from the aforementioned references that the Ahmed body is a well-accepted and recognized benchmark test case used by the computational fluid dynamics (CFD) community for the aerodynamic model validation of automobiles.

Severe weather can easily alter the aerodynamic flow properties of a ground vehicle, such as a utility truck with boom equipment, especially during heavy rainfall. When high-speed vehicles run under heavy rain and crosswind conditions, the aerodynamic forces and moments may increase significantly, resulting in the vehicle's instability. These weather conditions also hinder the driver's visibility, reduce the tire-road friction force, and further influence driving safety. Adverse weather always puts drivers and vehicles in critical hazardous conditions and increases the risk of accidents. The consequences of such alteration may result in severe road accidents, and thus, several authors

consistently accuse rain phenomena as the principal cause of weather-related accidents [11]-[16]. Therefore, it is essential to control the aerodynamic forces and moments of the utility truck under severe weather conditions. Even though the aerodynamic forces and moments are critical in the utility truck's stability under extreme weather conditions, there needs to be more information available in the literature addressing this issue. For example, Parth et al. [17]-[21] conducted the aerodynamic and dynamic analysis of the utility truck with the morphing boom equipment. But there is not much information available on the utility truck's aerodynamic performance in severe weather. Thus, the rain phenomenon is a matter of concern that needs to be analyzed from an aerodynamic perspective for the utility truck.

The present investigation studies the rain modelling effect on the Ahmed body for real-life conditions. What differs from previous studies is that the yaw angle of up to 55 degrees has been added as a variable to study the rain modelling effect. Additionally, the present work compares the bluff body's experimental testing and CFD simulations. Afterward, the impact of heavy rainfall (LWC= 30 g/m^3) on the external aerodynamics of the utility truck with the morphing boom equipment using the validated DPM based numerical method is presented.

III. Methodology

Methodologies for the wind tunnel experiments and the computational fluid dynamics numerical models will be presented next.

A. Wind Tunnel Experiments

An Ahmed body as shown in Figure 1 introduced by Ahmed et al. [4] is employed and modeled experimentally in the present study as the benchmark ground vehicle model. The Ahmed body has been modeled at a true automotive scale to generate essential features of the flow around the ground vehicle and avoid the Reynolds number effect. The Ahmed body model is 3 times larger than the model originally studied by Ahmed et al [4].

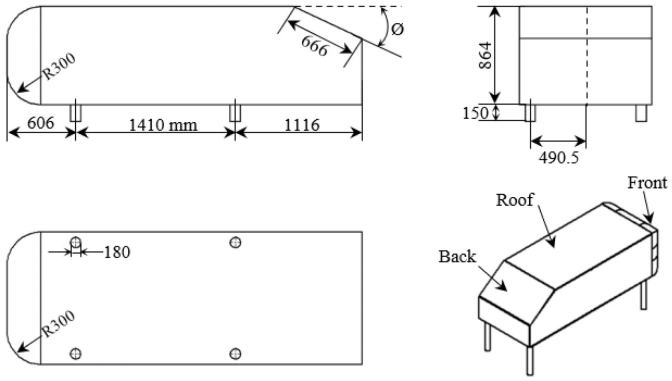

Figure 1. Geometry of Ahmed body

Florida International University (FIU), working under a Natural Hazards Engineering Community (NHERI), operates the Wall of Wind (WOW) Experimental Facility (EF) [22]. This facility is powered by a combined 12-fan system capable of repeatable testing up to 157 mph wind speeds through its flow management system. The unique advantage of the NHERI WOW EF is multi-scale (full-scale/large-scale) and high Reynold number simulation of the effects of wind and wind-driven rain, which is accomplished using 12-fans and a water spray system. The open test section is rectangular in a cross section with a width of 20 ft. and a height of 14 ft. It has a turntable with a diameter of 16 ft., where an actual testing model is placed. Vehicle drag, lift, and side forces can be measured using load cells. An outline of the experimental facility and the experimental setup of the Ahmed body is shown in Figure 2.

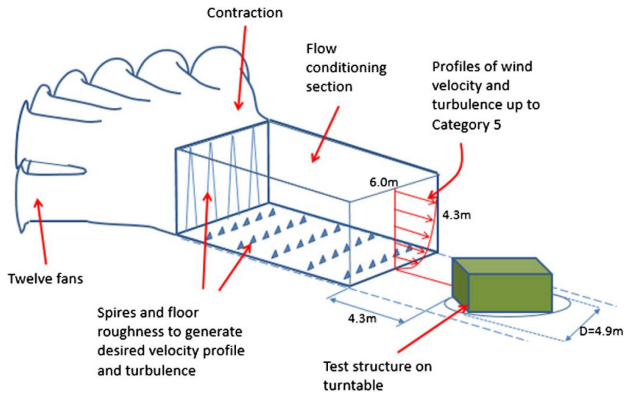

(a)

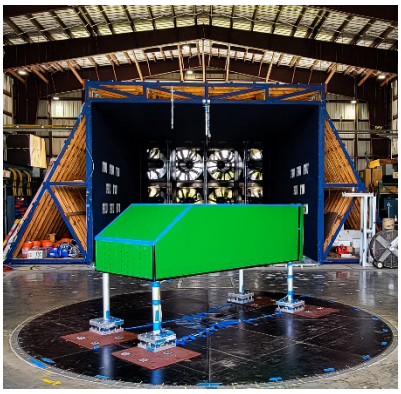

(b)

Figure 2. (a) Wall of Wind Experimental Facility (A. Gan Chowdhury et al. [23]) (b) Ahmed Body experimental setup (Image by Parth Y. Patel)

The frontal area to the test section area ratio, i.e., blockage ratio, is about 3.95 %, representing a minimal blockage [24]. The model was mounted on four poles representing stilts, as shown in Figure 2(b), at 0.635 m above the ground. It should be noted here that the positions of the stilts are different in the present study compared to the model studied by Ahmed et al. [4]. The drag, lift, and side force were measured using the load cells and has an estimated absolute uncertainty of ±0.25. Wind-driven rain setup at the WOW EF is shown in Figure 3. The WOW EF can induce 63 gallons/min of water into the wind field. Thus, 63 gallons/min (3.9747 kg/s) of water was injected during the wind-driven rain experiments with the wind speed of 85 mph (37.9984 m/s).

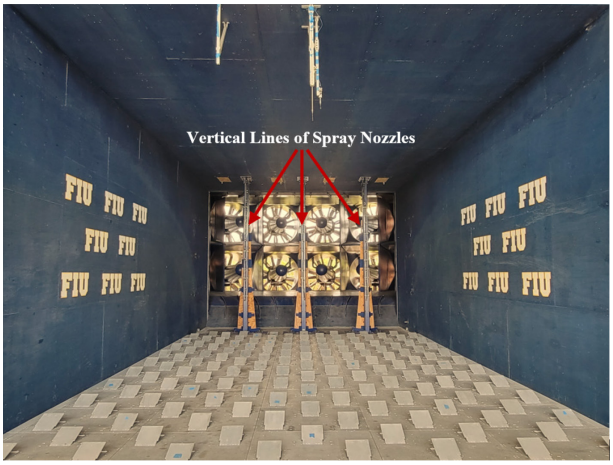

Figure 3. Wind-driven rain setup at WOW EF (Image by Parth Y. Patel)

B. Computational Fluid Dynamics

Details of the modelling of rain particles, numerical modelling using incompressible unsteady Reynold Averaged Navier Stokes (URANS) equations, and multi-phase flows are discussed in the following sections.

i. Modelling of Rain Particles

In the experimental or numerical simulation, the rainfall intensities are commonly specified in terms of Liquid Water Content (LWC) in the air. The relation between rainfall rate R (mm/h) to LWC (g/m^3) for the thunderstorm type rain is given by the relation [25]

$$LWC = 0.054R^{0.84} \tag{1}$$

and for light spread type rain, it is given by

$$LWC = 0.0889R^{0.84} \tag{2}$$

Typical values of LWC for medium intensity rain is 19 g/m^3 and heavy rain is 30 g/m^3 [25]. Another parameter that is important in the simulation of objects under rain condition is the terminal velocity. This influences the momentum that is imparted on the body during the impingement of rain droplets on the object. As the rain droplets fall through the atmosphere, it accelerates and as the velocity increases the drag force acting on the droplets also increases. At the terminal velocity, the gravitational force balances with the drag force and the raindrops stop accelerating. Markowitz [26] presented an equation to estimate the terminal velocity as a function of the diameter of the rain droplets as

$$V_T\left(\frac{m}{s}\right) = 9.58\left\{1 - exp\left[-\left(\frac{d(mm)}{1.77}\right)^{1.147}\right]\right\} \tag{3}$$

where, V_T is the terminal velocity in (m/sec), and d is the rain droplet size in mm.

ii. Numerical Modelling

The flow features around bluff bodies are typically unsteady in nature due to flow separation and vortex shedding, even for a steady incoming flow. Therefore, it is advisable to conduct the simulation in an unsteady mode and take a time average value of the parameters of interest from the simulation. One of the approaches for resolving the small-scale turbulent fluctuations in an unsteady flow field is the large eddy simulations (LES). However, this could be computationally expensive. Alternatively, the unsteady Reynolds averaged Navier Stokes (URANS) simulation is frequently used in the investigation of long-term periodical oscillations in a turbulent flow and this approach is adopted to conduct the simulations presented in this paper.

With the usual notations, the incompressible unsteady Reynolds Averaged Navier Stokes (URANS) equations is written as [27]

$$\frac{\partial \rho}{\partial t} + \frac{\partial(\rho u_i)}{\partial x_i} = 0 \tag{4}$$

$$\frac{\partial(\rho u_i)}{\partial t} + \frac{\partial(\rho u_i u_j)}{\partial x_j} = -\frac{\partial p}{\partial x_i} + \frac{\partial}{\partial x_j}\left[\mu\left(\frac{\partial u_i}{\partial x_j} + \frac{\partial u_j}{\partial x_i} - \frac{2}{3}\delta_{ij}\frac{\partial u_l}{\partial x_l}\right)\right] + \frac{\partial}{\partial x_j}\left(-\rho\overline{u_i' u_j'}\right) \tag{5}$$

The Reynolds stress appearing in the momentum equation can be written using the Boussinesq hypothesis as [27]

$$-\rho\overline{u_i' u_j'} = \mu_t\left(\frac{\partial u_i}{\partial x_j} + \frac{\partial u_j}{\partial x_i}\right) - \frac{2}{3}\left(\rho k + \mu_t\frac{\partial u_k}{\partial x_k}\right)\delta_{ij} \tag{6}$$

The eddy viscosity μ_t in the above equation is estimated using the two equations $k-\omega$ shear-stress transport (SST) turbulence model which is given by [27]

$$\mu_t = \frac{\rho k}{\omega}\frac{1}{\max\left[\frac{1}{\alpha^*}, \frac{SF_2}{a_1\omega}\right]} \tag{7}$$

where S is the strain rate magnitude, $a_1 = 0.31$ and α^* is a coefficient which is defined as [27]

$$\alpha^* = \alpha_\infty^*\left(\frac{\alpha_0^* + Re_t/R_k}{1 + Re_t/R_k}\right) \tag{8}$$

where

$$Re_t = \frac{\rho k}{\omega\mu} \tag{9}$$

$$R_k = 6 \tag{10}$$

$$\alpha_0^* = \frac{\beta_i}{3},\ \alpha_\infty^* = 1 \tag{11}$$

$$\beta_i = 0.072 \tag{12}$$

F_2 in equation 7 is given by

$$F_2 = tanh(\emptyset_2^2) \tag{13}$$

$$\emptyset_2 = \max\left[2\frac{\sqrt{k}}{0.09\omega y}, \frac{500\mu}{\rho y^2 \omega}\right] \tag{14}$$

where y is the distance to the next surface.

The advantage of using this turbulence model is that it considers the transport of the principal turbulence shear stress in the near wall region. The pressure-based flow solver available in ANSYS is used for the solution of the governing equations, which utilizes a finite volume method to discretize them. There are two pressure-based algorithms available in the ANSYS Fluent (i) a segregated algorithm, and (ii) a coupled algorithm [27]. In the segregated algorithm, each component of the governing equation is solved sequentially, and an iterative approach is used to achieve convergence at every time step. The segregated approach is memory efficient. However, the convergence rate is relatively slow in lieu of the equations are solved in a decoupled manner. The Coupled algorithm solves a coupled system of equations comprising the continuity equation and the momentum equations simultaneously. The convergence rate can be significantly improved in the coupled approach as compared to the segregated approach. In both these approaches, the turbulence model equations for the solution variable are solved one after another using a segregated algorithm.

iii. Multi-Phase Flow Approach

Currently, there are two main approaches available for the numerical calculation of the multi-phase flows: the Eulerian-Eulerian approach and the Eulerian-Lagrangian approach. In the Eulerian-Eulerian approach, the different phases are treated mathematically as separate continuous mediums. The concept of phase volume is introduced in this approach since the volume occupied by one phase cannot be occupied by another phases. An assumption is made for the volume fractions to be continuous in space and time, and their sum is equal to one. In this approach, the fluid phases are treated as continuum by solving the unsteady Reynolds Averaged Navier Stokes equations. In the Eulerian-Lagrangian approach, the under laying continuous medium is solved using the Eulerian approach and the dispersed phase is solved by tracking a large number of particles, bubbles, or droplets using a Lagrangian approach in the continuous medium. During these trajectory calculations, it is assumed that the dispersed phase can exchange momentum with the continuous phase. Additionally, we can simulate a discrete second phase consisting of spherical particles in a Lagrangian reference frame, and this model is called Discrete Phase Model (DPM). In order to simulate the rain environment, the DPM is employed in this paper. ANSYS Fluent [27] provides the capability to predict the trajectory of rain droplets by integrating the force balance on the particle, which is written in a Lagrangian reference frame. This balance of forces acting on the particle can be written as

$$\frac{d\vec{u}_p}{dt} = F_D\left(\vec{u} - \vec{u}_p\right) + \frac{\vec{g}\left(\rho_p - \rho\right)}{\rho_p} + \vec{F} \tag{15}$$

where $\vec{F}$ is an additional acceleration (force/unit particle mass), $F_D\left(\vec{u} - \vec{u}_p\right)$ is the drag force per unit particle mass, $\vec{u}$ is the fluid phase velocity, $\vec{u}_p$ is the particle velocity, ρ is the fluid density, ρ_p is the density of the particle, and F_D is defined as:

$$F_D = \frac{18\,\mu\,C_d\,Re}{\rho_p d_p^2\,24} \tag{16}$$

where, μ is the molecular viscosity of the fluid, C_d is drag coefficient, ρ is the fluid density, ρ_p is the density of the particle, d_p is the particle diameter, and Re is the relative Reynolds number, which is defined as

$$Re \equiv \frac{\rho d_p |\vec{u}_p - \vec{u}|}{\mu} \tag{17}$$

One of the parameters needed by ANSYS Fluent for DPM simulations is the mass flow rate of the DPM phase. In the following simulations, the DPM mass flow rates are specified at the inlet. To calculate the mass flow rate of the DPM phase, the volume flow rate is calculated using the product of the inlet area and the inlet velocity, and the resulting volume flow rate is multiplied by the rain intensity (LWC). For example, for an injection area of

30m×1m, the free stream velocity is 40 m/s, and the volume flow rate is 1200 m^3/s. For a medium rain intensity (LWC) of 19 g/m^3 the mass flow rate for DPM is 22.8 kg/s. Another parameter that is needed for DPM simulation is the size distribution of the dispersed medium. Based on the data available from the literature [28][29], the minimum, maximum, and mean diameter of the droplets are defined as 0.5 mm, 2.5 mm, and 1.5 mm, respectively. Finally, the two-way coupling between the continuous phase and discrete phase is used to simulate more accurate rain behavior.

iv. Computational Setup and Boundary Conditions

A computational domain is prepared according to the guidelines provided by Lanfrit [30] to manage the external aerodynamics. The refined mesh regions are defined to capture the wake zone properly and obtain precise results as shown in Figure 4. In this geometry, the origin of the coordinate system is placed at middle of the Ahmed body, with z = 0 middle of the model, x = 0 at the symmetric plane, and y = 0 at the ground plane. The mesh for the computational simulations is generated using ANSYS Fluent software. The mesh used for the simulations is composed of around 12.5 million elements. The law of wall states the proportionality of average flow velocity at a certain point and the logarithmic distance of the fluid boundary region [31]. According to this law, the viscous sublayer lies within $y^+<5$, the buffer layer is between $5< y^+<30$, and the rest is the logarithmic layer. In this setup, the resultant y^+ on the surface varies in the range of $1.13< y^+<28.9$. Therefore, the $y^+<30$ is chosen to capture the near-wall flow properties accurately.

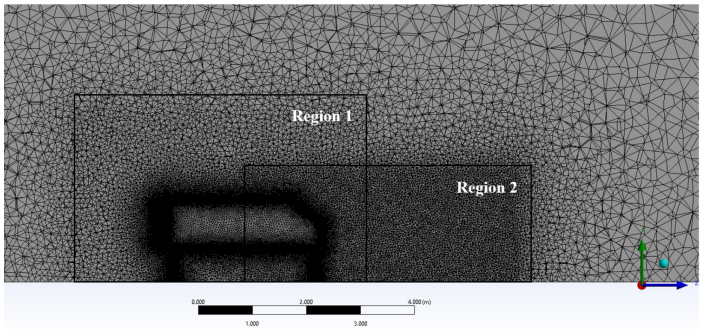

Figure 4. Near mesh of the Ahmed body

In these simulations, velocity inlet is taken as 29.629 m/s, which is the mean velocity computed from the experimental tests. Since the flow speed is less than Mach number 0.3, it is assumed that the flow is incompressible, and the density is set to constant value. For the solution of the governing equation, the time derivatives are discretized using first order and the spatial derivatives in the continuity and momentum equations are discretized using a second-order upwind method. A least-squares cell-based method is applied in the estimation of the gradients of the flow variables. A coupled numerical approach is used for the solution of the continuity and the momentum equations. Finally, a first-order upwind technique is applied for the solution of the turbulent kinetic energy and specific dissipation rate equations for the k-ω SST model.

An assumption is made that the velocity of water particles are same as the wind velocity, i.e., 29.629 m/s. For the DPM model, a reflect boundary condition with the polynomial of normal and tangential discrete phase reflection coefficients is specified at the Ahmed body, stilts, and on the ground. The normal coefficient defines the amount of momentum in the direction normal to the wall that is retained by the particle after the collision with the boundary. Similarly, the tangential coefficient defines the amount of momentum in the direction tangential to the wall that is retained by the particle. In addition, an escape boundary condition is defined at the inlet, outlet, and two sides. Simulations are conducted using the same rain intensity used while performing wind-driven rain experiments. Ansys Fluent does not take the force exerted by the DPM particles in the calculation of drag, lift, and side force coefficients using the built-in report definition functions. However, it reports the components of the forces exerted by DPM particles in each coordinate direction. These force components are used to estimate drag, lift, and side force coefficients due to DPM particle impingement and are added to the corresponding coefficients to get the total force coefficients.

IV. Experimental and Computational Results of Ahmed Body Aerodynamics

One of the essential steps in the computational simulations is estimating the accuracy of the computational results using experimental data. For aerodynamic applications, the approach to achieve this verification is computing and comparing the drag, lift and side force coefficients with the experimental data and numerical simulations. In this study, the computational modeling methodology for Discrete Phase Model (DPM) is validated using the experimental data which were derived from conducted experiments at WOW EF. Computational simulations and experimental tests were carried out for sideslip angles of 0^0 to 55^0 in steps of 5 degrees.

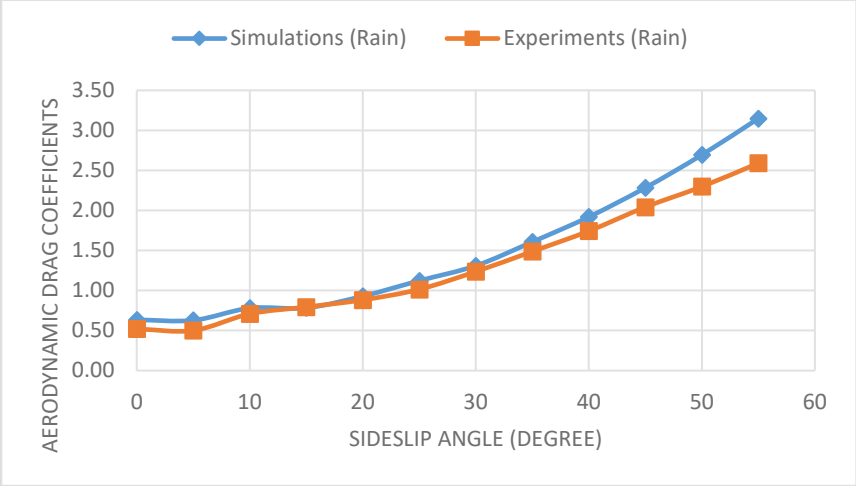

(a) Drag Coefficient

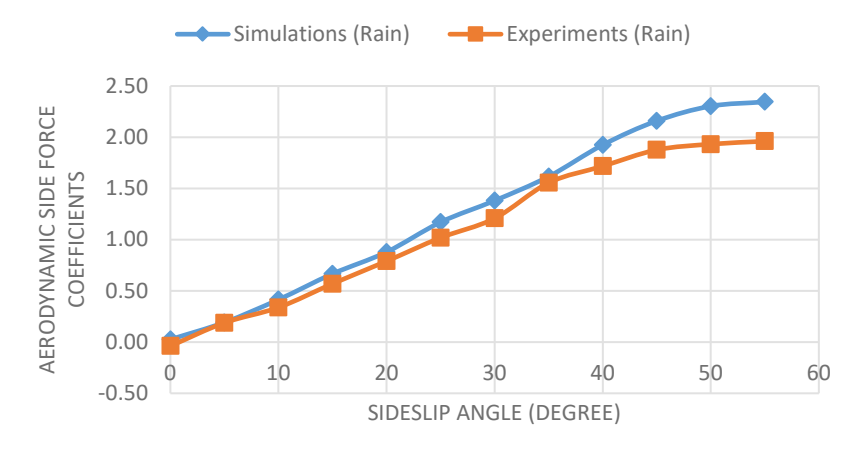

(b) Side Force Coefficient

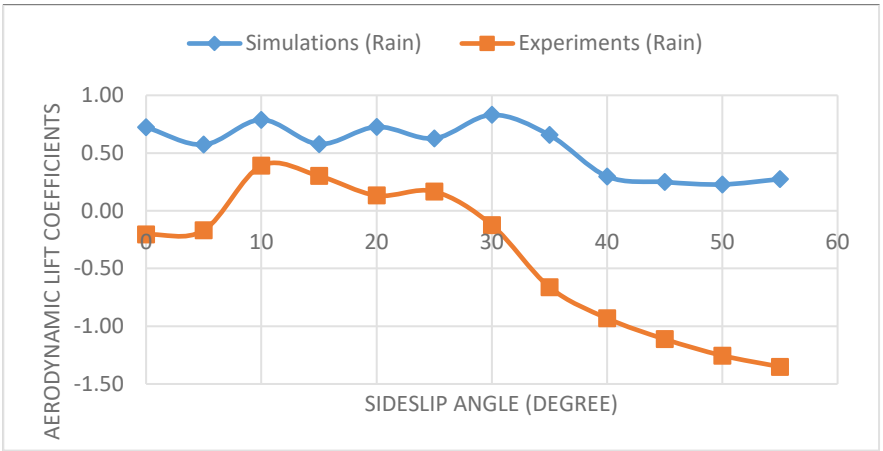

(c) Lift Coefficient

Figure 5. Comparison of force coefficients from present computational and experimental studies of the Ahmed Body

Figure 5 compares drag, lift, and side force coefficients from the experimental and numerical results of wind-driven rain of the Ahmed body. The present computational and experimental results of the drag and side force coefficient agree reasonably well. Both drag and side force coefficients increase as the sideslip angle increases. However, the lift coefficient does not go along with the experimental results, however it follows the trend, as shown in Figure 5(c). Several reasons might cause to deviate present computational results from the experimental results for the lift coefficient. We are currently investigating and addressing this issue with the testing facility. The difference between present computations and experimental measurements for the drag and side force coefficients is less than 10% to 40 degrees of yaw angle, increasing to 17% to 55 degrees. Flow that is separated from the body at 15^0 may not become attached over a different area than the body is yawed through 55^0 under continuous flow conditions. This effect is common in airfoil testing as an angle of attack increases beyond the stall and then decreases back to the value where the flow was previously attached [32]. The influence of the trailing vortex system may play a role in flow physics, and thus, some discrepancies can be seen in present computational and experimental results. It should be noted that no previous publication discusses the rain modelling of the Ahmed body with a back angle of 35^0. Therefore, no computational/experimental data is available to compare present results.

V. Computations of External Aerodynamics for the Utility Truck with the Morphing Boom Equipment

The computational results for the external aerodynamics of the utility truck with the morphing boom equipment are discussed in this section. Computational models, which was highlighted in the section II & III, are applied to a very complex geometry. The utility truck is a commercial vehicle outfitted with a boom, a hydraulic pole with a worker-carrying bucket at the end. When the boom morphs, this bucket assists the worker in safely performing the tasks and working comfortably with the tools. Figure 6 depicts the utility truck's configuration and component identification.

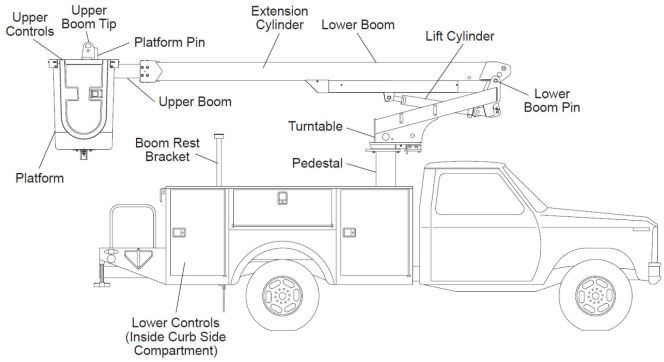

Figure 6. Configuration and component identification of the utility truck

The size of the computational domain is prepared according to the guidelines provided by Lanfrit [30] to manage the external aerodynamics around the utility truck as shown in Figure 7. The computational domain was divided into six parts: two side walls, top, ground, inlet, and outlet. The length of the computational domain was taken as 75 m, width was taken as 44 m and the height was taken as 21 m.

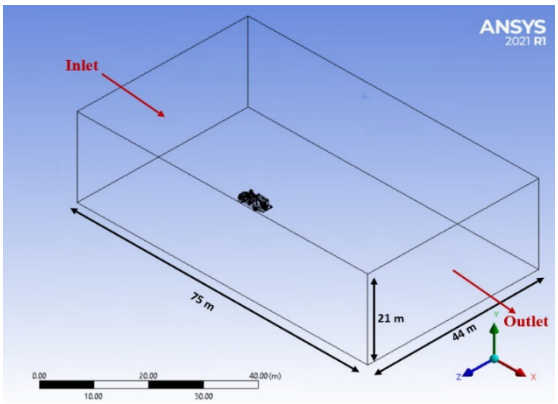

Figure 7. Computation domain with the utility truck

The computational domain mesh was discretized using a generalized mesh topology, and the boundary layer mesh was applied around the utility truck model, as shown in Figure 8. The generated mesh for the zero-degree sideslip angle consisted of around 17 million elements. To mimic different sideslip angles, the utility truck was rotated inside the computational domain, which resulted in a slightly different number of elements and nodes for different side slip angles. Thus, the resulting mesh will have a different elements and nodes at various sideslip angles. A refined mesh regions are defined to capture the wake zone properly and obtain precise results as shown in Figure 8. In this setup, the resultant y^+ on the surface varies in the range of $0.005 < y^+ < 50$. Therefore, the $y^+ < 50$ is chosen to capture the near-wall flow properties accurately. In this truck geometry, the origin of the coordinate system is placed according to the SAE aerodynamic reference point [33] as a wheelbase mid-point along the intersection of vehicle plane of symmetry and at the ground.

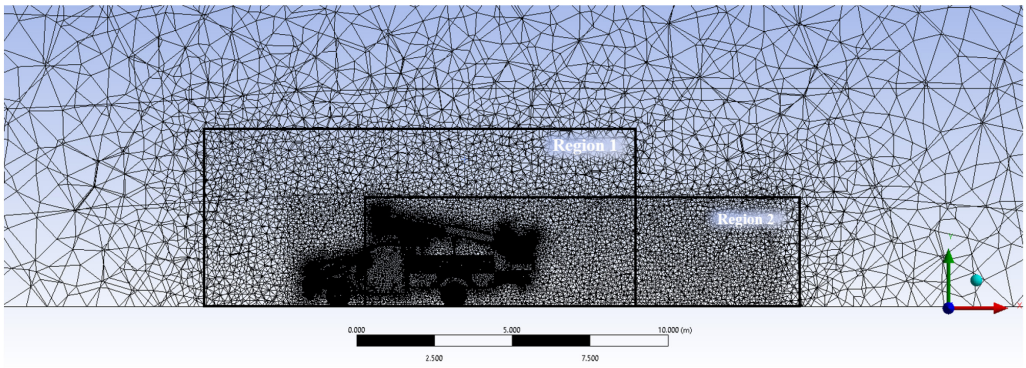

Figure 8. Near mesh of the utility truck with the boom equipment

Rain intensity of heavy rain, i.e., LWC = 30 g/m^3 [25], is used in these simulations to investigate the effect of heavy rain on the aerodynamic forces and moments. Again, the same DPM boundary conditions are specified as the one defined for the Ahmed body. Unsteady CFD simulations were performed using a step size of 0.001 seconds and each simulation was run for 1000-time steps. The residuals, force, and moment coefficients-plots were checked to make sure that the solution was stabilized, and the force and moment coefficients reached asymptotic values. Computational simulations were carried out for sideslip angles of 0 to 45 in steps of 5 degrees.

The static pressure distribution on the utility truck for these sideslip angles is shown in Figure 9. In these simulations, the static pressure distribution of the front and left sides of the truck ranged from -3544.942 to 1006.478 Pa, which is comparable to the static pressure distribution of wind only of the utility truck provided in [17]. The negative pressure areas were primarily at the top and right-side surfaces of the utility truck. In contrast, other areas directly facing the

wind-driven rain had increased positive pressure because of the rain particle impingement. The positive area at the cabin front and the boom equipment gradually shifts towards the left side due to the increased sideslip angle. Thus, it becomes more prominent, leading to the increased side force. Furthermore, the force exerted by the water particle impingement at the front of the cabin and the boom equipment causes the aerodynamic drag force on the utility truck to increase, which can be seen from the static pressure distribution.

The velocity contours without and with the rain around the utility truck at the zero-degree sideslip angle on the symmetry plane are shown in Figures 10 and 11, respectively. These figures show the complex separated flow pattern around the utility truck. In the case of air, when it reaches the end of the trailer and at the bucket, it separates from surfaces and causes a swirling flow behind the bucket. Furthermore, the air undercarriage of the trailer gets separated from the trailing end surface, which generates a small swirl underneath, as represented in Figures 10 and 11. However, the same flow behavior can be seen in the case of wind-driven rain, except the velocity and the swirl region reduces, as shown in Figure 11. A low-pressure region is created behind the bucket when the separation of the air occurs, which increases the drag force acting on the truck.

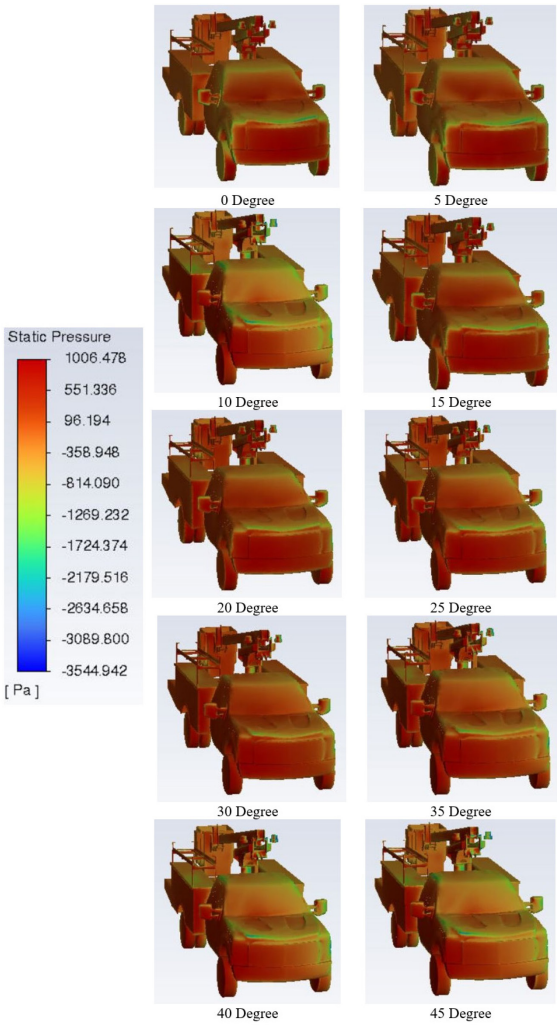

Figure 9. Static Pressure distribution on the utility truck

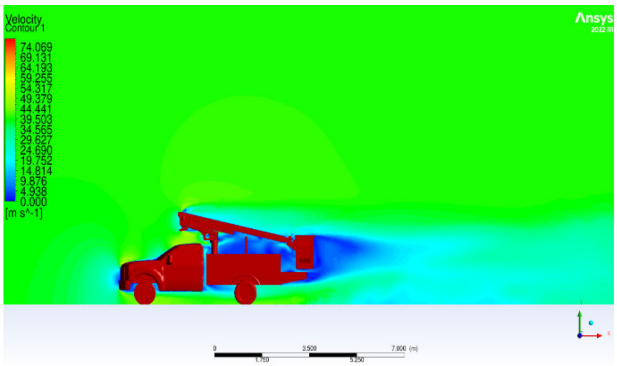

Figure 10. Velocity contours at the symmetry plane around the utility truck at 0^o sideslip angle (without rain)

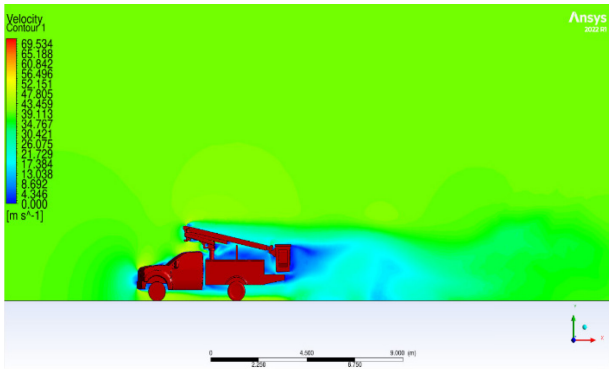

Figure 11. Velocity contours at the symmetry plane around the utility truck at 0^o sideslip angle (with rain)

When aerodynamic forces interact with the truck, it generates drag, lift, and lateral forces, and pitch, roll and yaw moments. The aerodynamic forces and moments are typically written in terms of the non-dimensional force and moment coefficients and the reference conditions defined as follows [34]

$$D_A = \frac{1}{2} C_D \, \rho A V^2 \tag{18}$$

$$L_A = \frac{1}{2} C_L \, \rho A V^2 \tag{19}$$

$$S_A = \frac{1}{2} C_S \rho A V^2 \quad (20)$$

$$PM = \frac{1}{2} C_{PM} \rho A V^2 L \quad (21)$$

$$RM = \frac{1}{2} C_{RM} \rho A V^2 L \quad (22)$$

$$YM = \frac{1}{2} C_{YM} \rho A V^2 L \quad (23)$$

where D_A is the drag force, L_A is the lift force, S_A is the side force, PM is the pitching moment, RM is the rolling moment, YM is the yawing moment, C_D is the drag coefficient, C_L is the lift coefficient, C_S is the side force coefficient, C_{PM} is the pitching moment coefficient, C_{RM} is the rolling moment coefficient, C_{YM} is the yawing moment coefficient, ρ is the density of the air, A is the frontal area of the truck, V is the total velocity of vehicle speed and wind speed, and L is the reference length.

In these calculations, the reference area is taken as 5.334077 m^2, reference length is taken as 1 m, reference velocity is taken as 40 m/s, and reference density is taken as 1.225 kg/m^3. For the calculation of the moments, the moment center is taken as the origin of the coordinate system. These forces and moments are calculated by CFD simulations for 10-sideslip angles. All the results of aerodynamic forces and moments with and without the rain are shown in Figures 12 and 13.

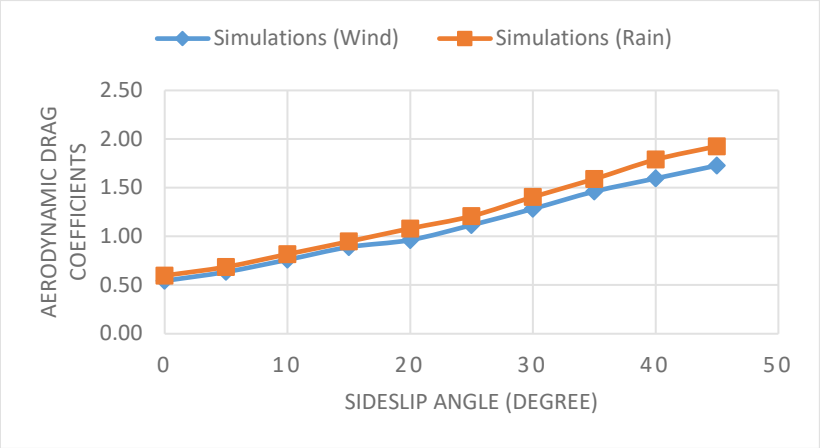

(a) Aerodynamic drag coefficients

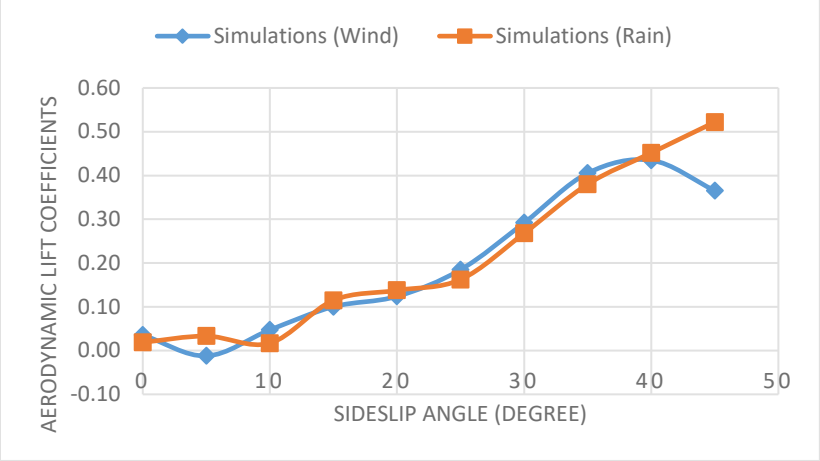

(b) Aerodynamic lift coefficients

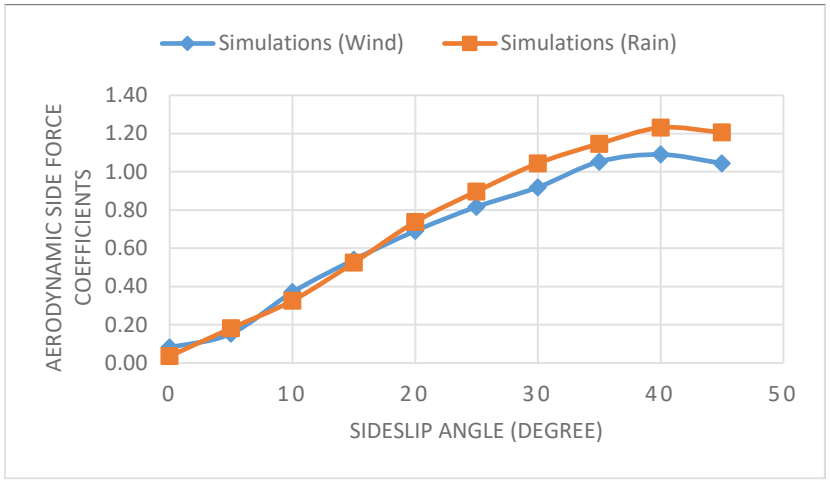

(c) Aerodynamic side force coefficients

Figure 12. Variation and comparison of force coefficients for different sideslip angles

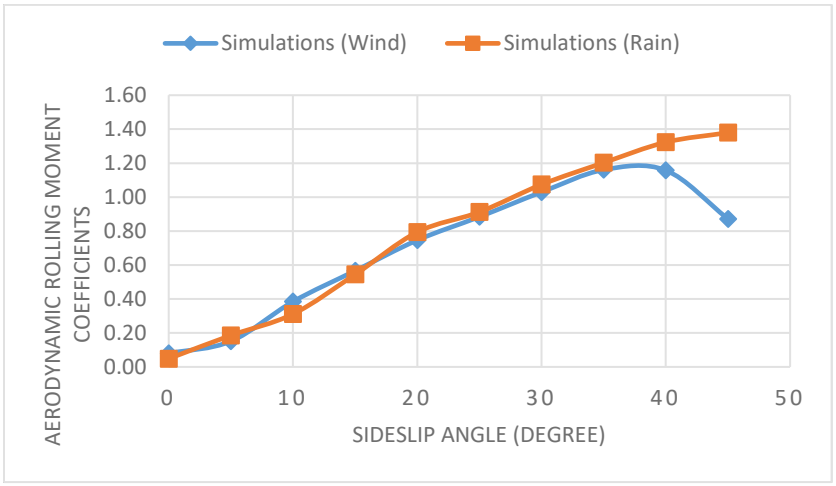

(a) Aerodynamic rolling moment coefficients

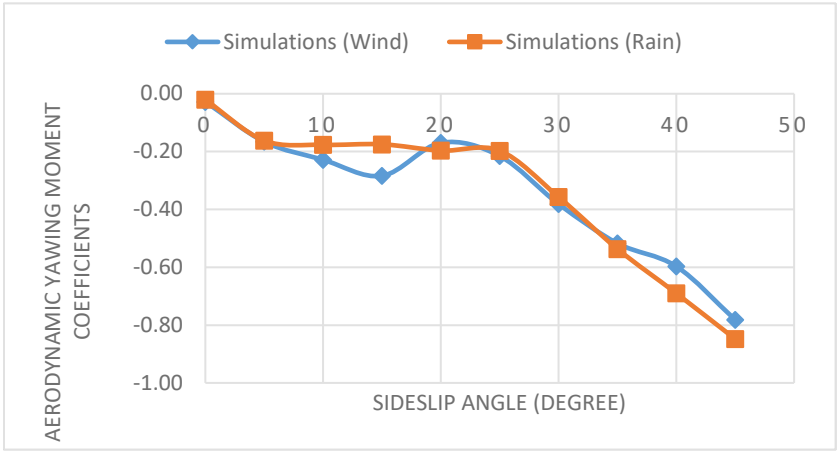

(b) Aerodynamic yawing moment coefficients

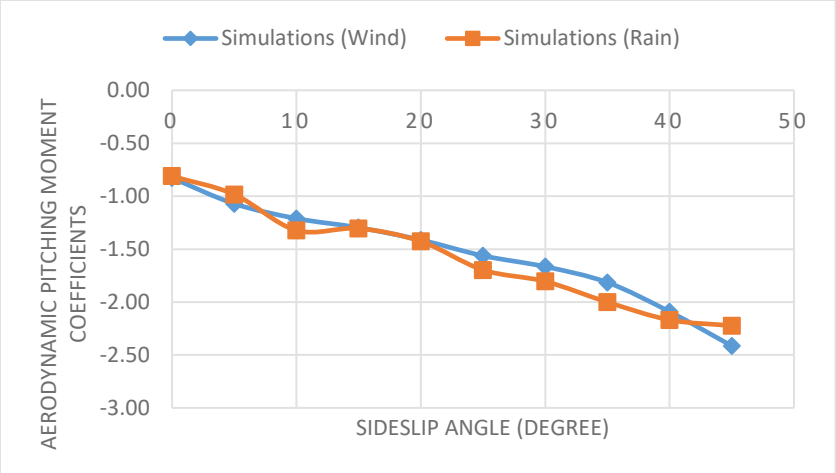

(c) Aerodynamic pitching moment coefficients

Figure 13. Variation and comparison of moment coefficients for different sideslip angles

The CFD simulations provide the aerodynamic drag coefficient values in the range of 0.54 – 1.73 (wind) & 0.59 – 1.92 (rain) for the range of 0^0 – 45^0 of sideslip angle. It can be inferred that the rain simulations produce a higher value of the drag coefficients because of the rain particle impingement on the front of the truck. Furthermore, more significant momentum changes of wind-driven rain hitting the trailer adds another more prominent drag component in crosswind conditions. Lift force depends on the vehicle's overall shape and pressure distribution underneath and on top of the vehicle. Water particle impingement adds weight to the vehicle, reducing the lift force to the wind simulations. Periodic behavior can be seen in the wind-driven rain simulations till the 20-degree sideslip angle, and then a reduction in the lift force can be seen, as shown in Figure 12(b). It is reported in the literature that the side force coefficient for automobiles is zero at zero relative wind angle, and it grows nearly linearly with the angle for the first 20 to 40 degrees from zero to one [34]. Similar behavior is also noted with the shift in wind-driven rain simulations, and the CFD simulations predicted linearity in the side force coefficients.

While the lift force decreases or increases the weight on the axles, the pitching moment transfers weight between the front and rear axles [34]. In the case of wind-driven rain, lift force reduces and thus, consequently, predicts the same behavior for the pitching moment. The yawing moment coefficient varies with wind direction, starting at zero with zero relative angles and growing almost linearly up to a 20-degree angle [34]. CFD simulations for the wind predict the same linearity till 20-degree and a shift in the value appears after 20 degrees, but it observes the linearity behavior. Wind-driven rain follows the same trend, but there's a slight variation between 10 to 20 degrees. The rolling moment is sensitive to wind direction, much like the yawing moment being quite linear over the first 20 degrees of sideslip angle [34]. Therefore, the same linearity with a slight shift in wind-driven rain is noticed in the predicted rolling moment coefficients.

VI. Conclusions

In this study, we experimentally and computationally investigated the rain effect on the aerodynamic behavior of the Ahmed body with 35^0 back angles. A DPM-based numerical approach was used for simulating rain and was validated using the experiments conducted at the Wall of Wind Experimental Facility (EF). Force coefficients were determined from both experimental and CFD measurements. It was observed that computational simulations predicted similar results compared to the experimental results except for the lift coefficient. Still, it follows the trend with the experimental results, which is under investigation to find the reason which causes this deviation. This validated model was used to study the effect of heavy rain on the external aerodynamics of the utility truck with the morphing boom equipment. The force and moment coefficients are computed for both wind & wind-driven rain and compared with each other. The static pressure distribution is also plotted to visualize the pressure distributions for the various sideslip angles. The present validated computational numerical approach can be used and applied for the external aerodynamic analysis of an automobile under heavy rain.

Acknowledgments

This research work is supported by NSF award S&AS-1849264. The authors gratefully acknowledge the resources provided by the University of Alabama at Birmingham IT-Research Computing group for high performance computing support (HPC) and CPU time on the Cheaha compute cluster. We would like to express our gratefulness to Altec Inc., our research partner for providing CAD geometry of the utility truck and required data for the research analysis, which aided us to progress in our research. Also, we would like to thank Inchan Yoon, an undergraduate student at the University of Alabama at Birmingham for helping us in running computational simulations.

References

[1] Climate Science Special Report, URL: https://science2017.globalchange.gov/chapter/7/

[2] "Freight facts and figures 2015, US department of transportation, bureau of transportation statistics,". URL: http://www.princeton.edu/~alaink/Orf467F16/FHWA2201FreightFactsF_complete.pdf/.

[3] Bonitz, S., L. Larsson, L. Löfdahl, and S. Sebben, "Numerical Investigation of Crossflow Separation on the A-Pillar of a Passenger Car," Journal of Fluids Engineering, 2018. 140(11). doi: https://doi.org/10.1115/1.4040107

[4] S. R. Ahmed, G. Ramm, and G. Faltin. Some salient features of the time averaged ground vehicle wake. SAE Paper 840300, 1984. doi: https://doi.org/10.4271/840300

[5] Bayraktar, I., D. Landman, and O. Baysal, "Experimental and computational investigation of Ahmed body for ground vehicle aerodynamics," SAE transactions, 2001: p. 321-331. doi: https://doi.org/10.4271/2001-01-2742

[6] H. Lienhart and S. Becker. Flow and turbulence structure in the wake of a simplified car model. SAE Paper 2003-01-0656, 2003. doi: https://doi.org/10.1007/978-3-540-45466-3_39

[7] Mathey, F. and D. Cokljat, Zonal multi-domain RANS/LES simulation of airflow over the Ahmed body, in Engineering Turbulence Modelling and Experiments 6. 2005, Elsevier. p. 647-656. doi: https://doi.org/10.1016/B978-008044544-1/50062-5

[8] Fares, E., "Unsteady flow simulation of the Ahmed reference body using a lattice Boltzmann approach," Computers & fluids, 2006. 35(8-9): p. 940-950. doi: https://doi.org/10.1016/j.compfluid.2005.04.011

[9] Minguez, M., R. Pasquetti, and E. Serre, "High-order large-eddy simulation of flow over the "Ahmed body" car model," Physics of fluids, 2008. 20(9): p. 095-101. doi: https://doi.org/10.1063/1.2952595

[10] Parth Y. Patel, Jia H. Liu, Vladimir V. Vantsevich and Roy P. Koomullil. "Modelling Effect of Rain on Aerodynamic Performance of the Ahmed Body," AIAA 2022-0335. AIAA SCITECH 2022 Forum. January 2022. doi: https://doi.org/10.2514/6.2022-0335

[11] Qiu, L., and W.A. Nixon, "Effects of adverse weather on traffic crashes: systematic review and meta-analysis," Transportation Research Record, 2008. 2055(1): p. 139-146. doi: https://doi.org/10.3141/2055-16

[12] Edwards, J.B., "Weather-related Road accidents in England and Wales: a spatial analysis," Journal of Transport Geography, 1996. 4(3): p. 201-212. doi: https://doi.org/10.1016/0966-6923(96)00006-3

[13] Edwards, J.B., "The temporal distribution of road accidents in adverse weather," Meteorological applications, 1999. 6(1): p. 59-68. doi: https://doi.org/10.1017/S1350482799001139

[14] Jaroszweski, D. and T. McNamara, "The influence of rainfall on road accidents in urban areas: A weather radar approach," Travel behaviour and society, 2014. 1(1): p. 15-21. doi: https://doi.org/10.1016/j.tbs.2013.10.005

[15] Elvik, R., "Laws of accident causation," Accident Analysis & Prevention, 2006. 38(4): p. 742-747. doi: https://doi.org/10.1016/j.aap.2006.01.005

[16] Changnon, S.A., "Effects of summer precipitation on urban transportation," Climatic Change, 1996. 32(4): p. 481-494. doi: https://doi.org/10.1007/BF00140357

[17] Patel, PY, Jannoi, T, Zou, W, Vantsevich, V, & Koomullil, R. "Aerodynamic Analysis of the Utility Truck With the Morphing Boom Equipment." *Proceedings of the ASME 2022 Fluids Engineering Division Summer Meeting. Volume 2: Multiphase Flow* (MFTC); Computational Fluid Dynamics (CFDTC); Micro and Nano Fluid Dynamics (MNFDTC). Toronto, Ontario, Canada. August 3–5, 2022. V002T05A033. ASME. doi: https://doi.org/10.1115/FEDSM2022-88368

[18] Patel, P., Vantsevich, V., Happawana, G., Harned, C. et al., "Dynamic Formulation of the Utility Truck with the Morphing Boom Equipment," SAE Technical Paper 2022-01-0917, 2022,

doi: https://doi.org/10.4271/2022-01-0917.
[19] Patel, P.Y., Vantsevich, V., Koomullil, R. (2022). Inverse Dynamics of the Utility Truck's Morphing Robotic Manipulator. In: Larochelle, P., McCarthy, J.M. (eds) Proceedings of the 2022 USCToMM Symposium on Mechanical Systems and Robotics. USCToMM MSR 2022. Mechanisms and Machine Science, vol 118. Springer, Cham.
doi: https://doi.org/10.1007/978-3-030-99826-4_13
[20] Patel, PY, Happawana, G, Vantsevich, VV, Boger, D, & Harned, C. "Morphing Capabilities and Safe Operation Zone of the Utility Truck Boom Equipment." Proceedings of the ASME 2020 International Mechanical Engineering Congress and Exposition. Volume 7B: Dynamics, Vibration, and Control. Virtual, Online. November 16–19, 2020. V07BT07A025. ASME.
doi: https://doi.org/10.1115/IMECE2020-24283
[21] Parth Y. Patel, V. V. Vantsevich, Jordan Whitson, "Utility Truck: Morphing Boom Equipment for Terrain Mobility", 20th International Conference and 9th Americas Conference of ISTVS 2021. ISBN: 978-1-942112-52-5
[22] "NSF Announces Natural Hazards Engineering Research Infrastructure (NHERI) Experimental Facility Award – Wall of Wind (WOW) Facility at FIU receives $4.1 million NSF Award". September 24, 2015. Archived from the original on September 25, 2015. Retrieved February 2, 2016.
[23] Large-Scale Experimentation Using the 12-Fan Wall of Wind to Assess and Mitigate Hurricane Wind and Rain Impacts on Buildings and Infrastructure Systems A. Gan Chowdhury, A.M. ASCE; I. Zisis, A.M. ASCE; P. Irwin, F. ASCE; G. Bitsuamlak, A.M. ASCE; J.-P. Pinelli, A.M. ASCE; B. Hajra, A.M. ASCE; and M. Moravej, S.M. ASCE
doi: https://doi.org/10.1061/(ASCE)ST.1943-541X.0001785
[24] Hucho, W. H., 1998, Aerodynamics of Road Vehicles, SAE Publishing, Warrendale, PA.
doi: https://doi.org/10.1016/C2013-0-01227-3
[25] Bezos, G. M., Dunham Jr, R. E., Gentry Jr, G. L., & Melson Jr, W. E. (1992). Wind tunnel aerodynamic characteristics of a transport-type airfoil in a simulated heavy rain environment
[26] Markowitz, A. M., "Raindrop Size Distribution Expression," Journal of Applied Meteorology, Vol. 15, 1976, pp. 1029-1031. URL: http://www.jstor.org/stable/26177317.
[27] ANSYS Fluent Theory Guide, 2022R1, January 2022.
[28] S. Niu, X. Jia, J. Sang, X. Liu, C. Lu, and Y. Liu, "Distributions of raindrop sizes and fall velocities in a semiarid plateau climate: convective versus stratiform rains," Journal of Applied Meteorology and Climatology, vol. 49, no. 4, pp. 632–645, 2010.
doi: https://doi.org/10.1175/2009JAMC2208.1
[29] Tokay, A., A. Kruger, and W. Krajewski, Comparison of drop-size distribution measurements by impact and optical disdrometers, J. Appl. Meteorol., 40, 2083– 2097, 2001.
doi: https://doi.org/10.1175/1520-0450(2001)040<2083:CODSDM>2.0.CO;2
[30] Lanfrit, M., "Best practice guidelines for handling Automotive External Aerodynamics with FLUENT. 2005, Version.
[31] Von Kármán, T., "Mechanische änlichkeit und turbulenz," Nachrichten von der Gesellschaft der Wissenschaften zu Göttingen, Mathematisch-Physikalische Klasse, 1930. 1930: p. 58-76.
[32] Abbot, I. H. and von Doenhoff, A. E., Theory of Wing Section: Including a Summary of Airfoil Data, Dover Publication, New York, 1959. ISBN: 0486605868
[33] SAE J1939-21:2011. Surface vehicle recommended practice. The engineering society for advancing mobility land sea air and space.
[34] Gillespie, Thomas D. 1992. Fundamentals of Vehicle Dynamics. Premiere Series Books. Warrendale: SAE International.